ACS NANO
Cite This: ACS Nano 2018, 12, 9300−9308
www.acsnano.org

ARTICLE

Bioengineered H-Ferritin Nanocages for Quantitative Imaging of Vulnerable Plaques in Atherosclerosis

Minmin Liang,[†,#] Hui Tan,[‡,#] Jun Zhou,[‡] Tao Wang,[§] Demin Duan,[†] Kelong Fan,[†] Jiuyang He,[†] Dengfeng Cheng,[*,‡] Hongcheng Shi,[*,‡] Hak Soo Choi,[*,∥] and Xiyun Yan[*,†]

[†]Key Laboratory of Protein and Peptide Pharmaceutical, Institute of Biophysics, Chinese Academy of Sciences, Beijing 100101, China

[‡]Department of Nuclear Medicine, Zhongshan Hospital, Fudan University/Shanghai Institute of Medical Imaging, Shanghai 200032, China

[§]Peking University Third Hospital, Beijing 100191, China

[∥]Gordon Center for Medical Imaging, Department of Radiology, Massachusetts General Hospital and Harvard Medical School, Boston, Massachusetts 02114, United States

Supporting Information

ABSTRACT: **Inflammation and calcification concomitantly drive atherosclerotic plaque progression and rupture and are the compelling targets for identifying plaque vulnerability. However, current imaging modalities for vulnerable atherosclerotic plaques are often limited by inadequate specificity and sensitivity. Here, we show that natural H-ferritin nanocages radiolabeled with technetium-99m (^{99m}Tc-HFn) can identify and accurately localize macrophage-rich, atherosclerotic plaques in living mice using combined SPECT and CT. Focal ^{99m}Tc-HFn uptake was observed in the atherosclerotic plaques with multiple high-risk features of macrophage infiltration, active calcification, positive remodeling, and necrosis on histology and in early active ongoing lesions with intense macrophage infiltration. The uptake of ^{99m}Tc-HFn in plaques enabled quantitative measuring of the dynamic changes of inflammation during plaque progression and anti-inflammation treatment. This strategy lays the foundation of using bioengineered endogenous human ferritin nanocages for the identification of vulnerable and early active plaques as well as potential assessment of anti-inflammation therapy.**

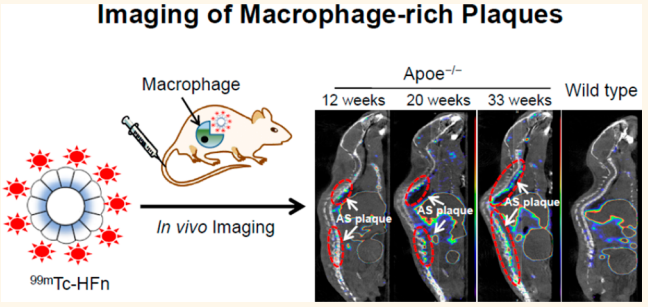

KEYWORDS: *atherosclerosis, vulnerable plaque, H-ferritin, SPECT imaging, PET imaging*

Atherosclerotic plaque rupture results in thrombus formation and vessel occlusion and is the leading cause of death worldwide.[1] Many infarcts originate from nonobstructive vulnerable plaque that cannot be identified by conventional diagnostic modalities, such as stress testing or aortic angiography, making it difficult to predict such vascular events.[2,3] Since the major determinants for acute clinical events are found to be the biological compositions of atherosclerotic plaques rather than the degree of stenosis,[2−4] the primitive approach in identifying such active biological compositions associated with high-risk plaques is the use of modern molecular imaging techniques in conjunction with targeted imaging agents.[5−8] Of these high-risk plaque compositions, inflammation and calcification concomitantly drive atherosclerotic plaque progression and rupture and are compelling targets for identifying plaque vulnerability.[9−12] To date, molecular imaging of vascular inflammation with ^{18}F-fluorodeoxyglucose (^{18}F-FDG) and calcification activity with ^{18}F-sodium fluoride (^{18}F-NaF) has been widely investigated for identifying vulnerable plaque.[13−18] Particularly, ^{18}F-FDG is also currently proposed as the noninvasive gold standard for atherosclerotic plaque vulnerability identification through detecting vascular inflammation and macrophage burden.[15,16] However, its clinical impact has been minimal because the high myocardial metabolic uptake of ^{18}F-FDG renders the interpretation of the signal as originating from coronary plaques.[17,18] In addition, the limited spatial resolution of PET (∼2 mm) and the small size of vascular plaques consequently require a high degree of focal ^{18}F-FDG accumulation. This is a

Received: June 1, 2018
Accepted: August 30, 2018
Published: August 30, 2018

DOI: 10.1021/acsnano.8b04158
ACS Nano 2018, 12, 9300−9308

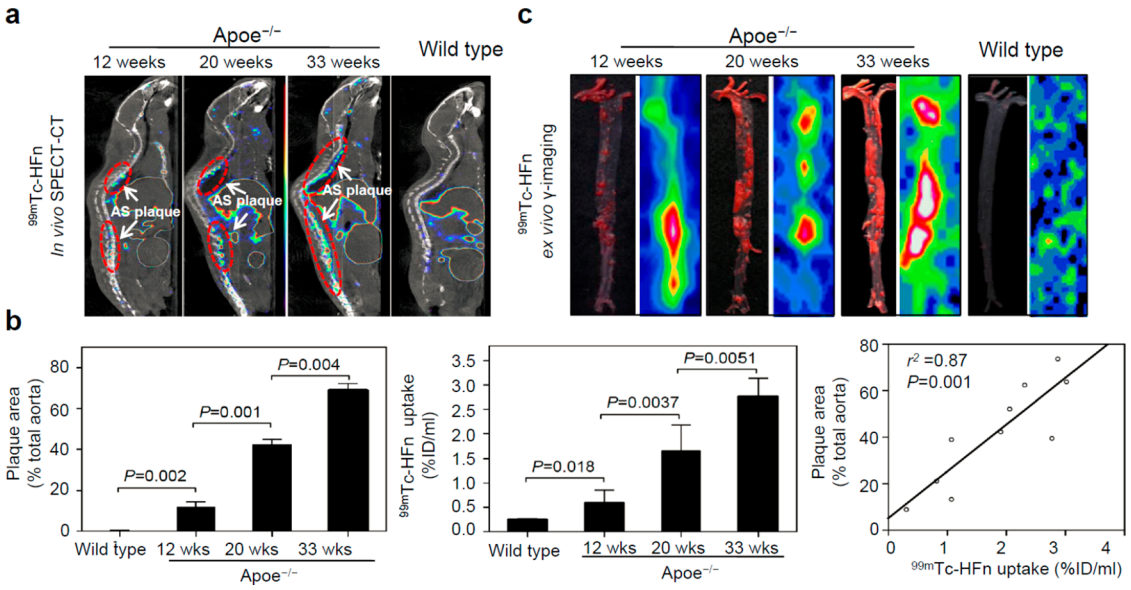

Figure 1. ***In vivo*** **and** ***ex vivo*** **imaging of atherosclerotic plaques with ^{99m}Tc-HFn. (a) Representative images of ^{99m}Tc-HFn SPECT-CT imaging in atherosclerotic and control mice. Red circles indicate atherosclerotic (AS) plaques. (b) Quantitative image analysis showing a high correlation between ^{99m}Tc-HFn uptake in aortas and the plaque area measured by Oil Red O staining (Pearson's correlation) (n = 8, mean ± SD; the comparisons were performed between two groups, and significance was evaluated by unpaired Student's t test). (c) Representative** ***ex vivo*** **planar images of the aortas excised from the mice after imaging with ^{99m}T-HFn and their corresponding representative Oil Red O staining images.** ***Ex vivo*** **images show colocalization of ^{99m}Tc-HFn uptake (yellow-red) to the site of atherosclerotic plaques (Oil Red O staining-positive areas) in the excised aortas.**

challenge owing to the limited specificity of ^{18}F-FDG imaging based on regional differences in plaque glucose metabolism.[17] Potentially more specific radiotracers for inflammation and better-suited for vascular lesions imaging are highly sought after for atherosclerosis characterization.

Ferritin is a self-assembled spherical iron storage protein nanocage composed of 24 subunits of two types: heavy-chain ferritin (HFn) and light-chain ferritin (LFn).[19−21] Increased levels of HFn proteins have been found to accumulate in the macrophages infiltrated into human atherosclerotic plaques.[22,23] Natural HFn may therefore reflect atherosclerotic progression *via* reporting macrophage accumulation within plaques. McConnel and colleagues examined the feasibility of using human ferritins for imaging vascular macrophages after conjugating with fluorophores or encapsulated magnetite nanoparticles.[24] We recently reported that human HFn specifically binds to tumor cells *via* transferrin receptor 1 (TfR1),[25−27] which is highly expressed in the infiltrated macrophages within atherosclerotic plaques and significantly associated with the increasing risk of plaque rupture.[22] We therefore investigated the use of bioengineered human HFn radiolabeled with ^{99m}Tc (^{99m}Tc-HFn) to identify vulnerable atherosclerotic plaques *in vivo* and validated its specific activity by comparison with the current noninvasive gold standard ^{18}F-FDG and the promising calcification activity imaging agent ^{18}F-NaF.

RESULTS

^{99m}Tc-HFn Images Vulnerable Atherosclerotic Plaques *in Vivo*. Bioengineered human HFn nanocages were prepared as described previously.[25−27] ^{99m}Tc-HFn was prepared by the radiolabeling of HFn with ^{99m}Tc using *N*-hydroxysuccinimide ester MAG_3 as an intermediate chelator (Supplementary Figure S1a), the radiochemical purity of which was confirmed by thin-layer chromatography (>98%; Supplementary Figure S1b). After purification, the prepared ^{99m}Tc-HFn nanocages were characterized by cryo-electron microscopy (cryo-EM) and dynamic light scattering (DLS). ^{99m}Tc-HFn shows a well-defined morphology and is monodisperse with an outer hydrodynamic diameter of ∼16 nm (Supplementary Figure S1c). The labeling stability of ^{99m}Tc-HFn was measured by monitoring ^{99m}Tc release over the course of incubation in fetal bovine serum at 37 °C. A radiochemical purity of >80% was detected after 12 h of serum incubation (Supplementary Figure S2), suggesting that ^{99m}Tc-HFn is stable enough during systemic circulation that it allows sufficient time for specific target uptake.

We evaluated the feasibility of atherosclerotic imaging with ^{99m}Tc-HFn in apolipoprotein E-deficient mice (Apoe$^{-/-}$) fed with a high-fat diet for 12, 20, or 33 wk, respectively, to develop varying degrees of atherosclerotic plaque buildup. Wild-type C57 mice were used as disease controls. The progressive development of atherosclerotic plaques in Apoe$^{-/-}$ mice was confirmed by Oil Red O staining of the aortas excised from Apoe$^{-/-}$ mice (Supplementary Figure S3).

We performed single-photon emission computed tomography/computed tomography (SPECT-CT) imaging 2 h postintravenous administration of ^{99m}Tc-HFn in atherosclerotic and control mice. As shown in Figure 1a, intense focal radiotracer uptake was observed in the aortas of atherosclerotic mice, whereas only scant uptake in the control mice was observed. As the atherosclerosis progressed, the radiotracer uptake in the aortas of atherosclerotic mice increased constantly from 0.597 ± 0.262%ID/mL at 12 wk to 1.659 ± 0.526%ID/mL at 20 wk and 2.767 ± 0.379%ID/mL at 33 wk, strongly correlated with the corresponding plaque areas quantified by aortic Oil-Red O staining (r^2 = 0.87, ***P = 0.001) (Figure 1b). This result demonstrates the feasibility of imaging atherosclerotic plaques with ^{99m}Tc-HFn.

DOI: 10.1021/acsnano.8b04158
ACS Nano 2018, 12, 9300−9308

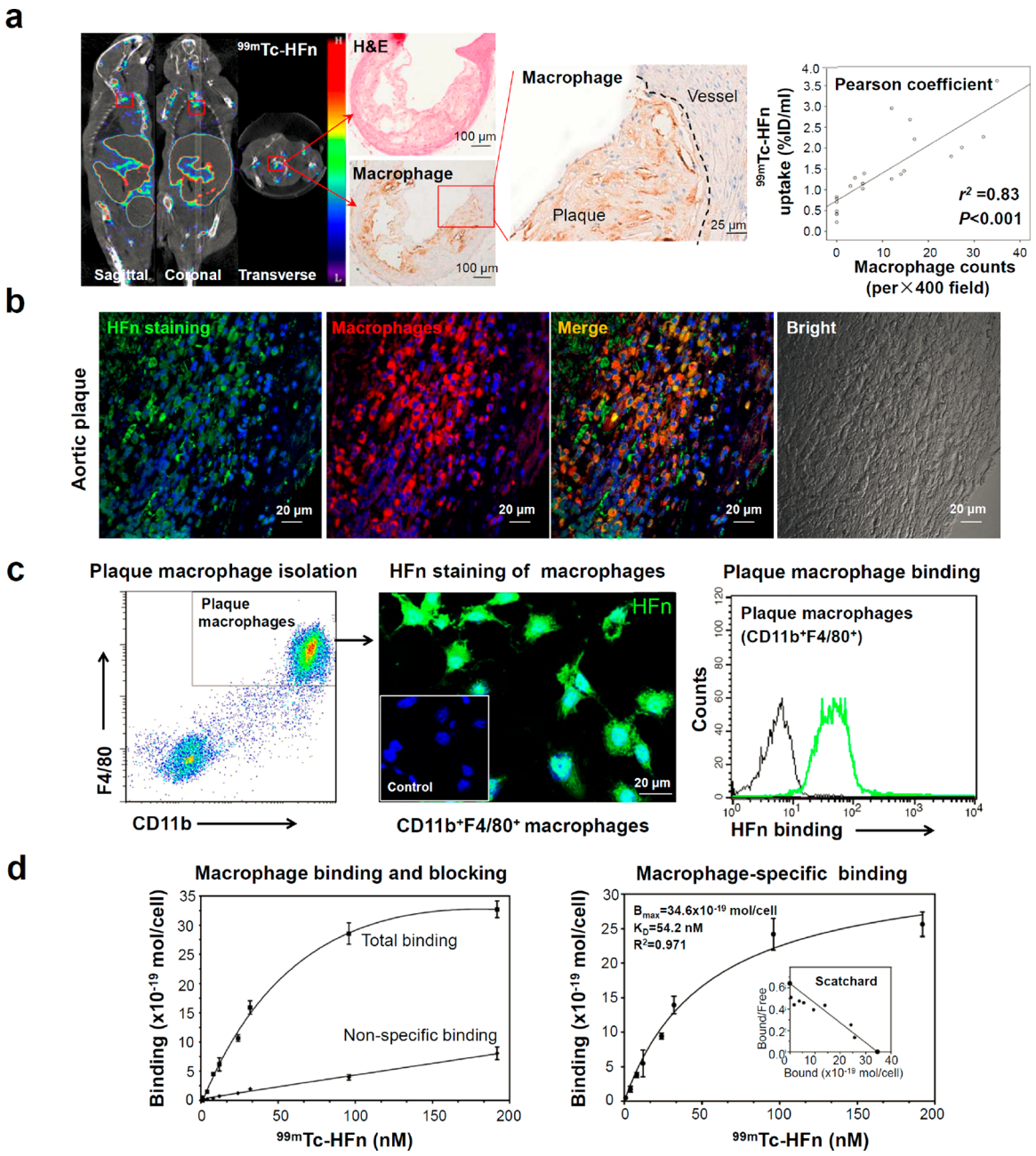

Figure 2. ^{99m}Tc-HFn accumulated in atherosclerotic plaques *via* specific binding to plaque-infiltrated macrophages. (a) Histology of the ^{99m}Tc-HFn-positive plaque region from the excised aorta showed intense macrophage infiltration (Mac-3 staining) and quantitative analysis showed high correlation between ^{99m}Tc-HFn uptake and the extent of macrophage infiltration within plaques (***$P < 0.001$, $r^2 = 0.83$; Pearson's correlation). (b) Immunofluorescent staining of ^{99m}Tc-HFn-positive plaque region demonstrated colocalization of HFn staining with macrophages (Mac-3 staining) within plaques. (c) Plaque-infiltrated CD11b$^+$F4/80$^+$ macrophages were isolated from aortic plaques (left) and were specifically stained by FITC-labeled HFn (H-ferritin), but not by FITC-labeled LFn (L-ferritin) in the control (middle). Flow cytometry analysis further confirmed the binding specificity of HFn to plaque macrophages (right). (d) Saturation binding curve for ^{99m}Tc-HFn to plaque macrophages. The total binding of ^{99m}Tc-HFn was measured by incubating macrophages with increasing amounts of ^{99m}Tc-HFn, and nonspecific binding was determined by adding 30-fold molar excess of nonradiolabeled HFn (left). Specific binding was obtained after subtraction of nonspecific binding from the total binding (right). Binding of ^{99m}Tc-HFn to plaque macrophages was saturable and could be blocked by adding an excess of unlabeled HFn, further confirming the macrophage specificity of HFn.

After *in vivo* imaging, the mice were sacrificed, and *ex vivo* planar imaging of the excised aortas was performed through gamma imaging. As shown in Figure 1c, intense radioactivity uptake (yellow-red) was localized to the sites of atherosclerotic plaques (Oil Red O staining-positive areas) in all Apoe$^{-/-}$ mice. No atherosclerotic plaques or specific radioactivity accumulation was present in aortas of control mice.

After *ex vivo* imaging, we characterized the ^{99m}Tc-HFn-positive region using histology. As shown in Supplementary Figure S4, focal ^{99m}Tc-HFn uptake occurred at the plaque region, showing histological evidence of intense macrophage infiltration (Mac-3 staining), active calcification (von Kossa staining), positive remodeling, thin fibrous cap (≤65 μm), and large necrotic cores (H&E staining) in morphology, indicating

DOI: 10.1021/acsnano.8b04158
ACS Nano 2018, 12, 9300−9308

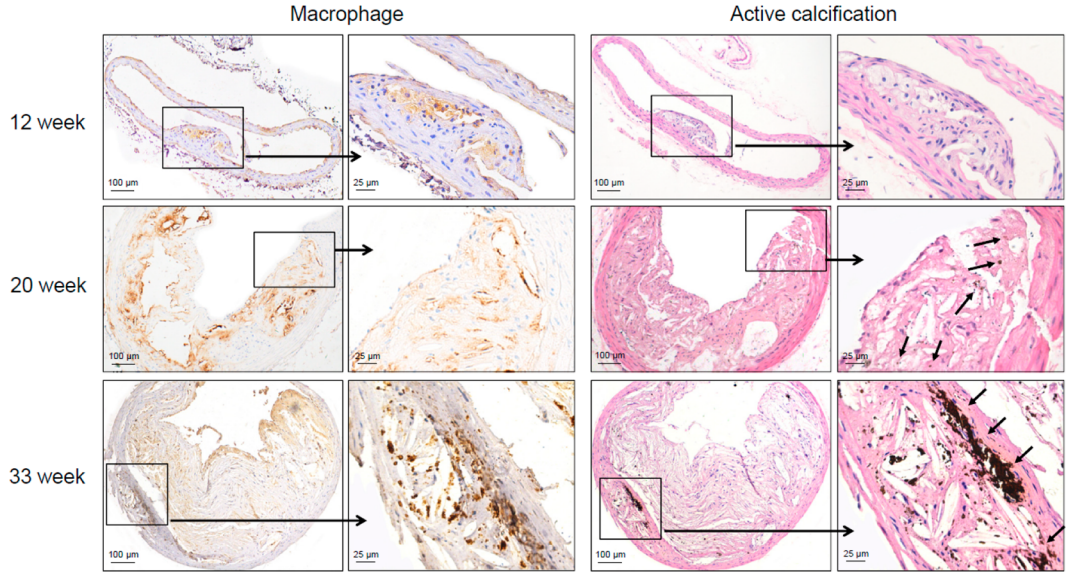

Figure 3. Inflammatory infiltration and calcification activity within progressive plaques. Representative serial sections of each group were detected by anti-Mac-3 antibody for macrophages and von Kossa staining for active calcifications. Early plaques (12 wk plaques) show no evidence of active calcification while yielding marked macrophage staining. Prominent calcification and macrophage infiltration are present in advanced plaques (20 and 33 wk plaques). Arrows in the right panel indicate calcific deposits (right panel).

the formation of high-risk atherosclerotic plaques. These results show that ^{99m}Tc-HFn images vulnerable plaques.

We then demonstrated that ^{99m}Tc-HFn accumulated into atherosclerotic plaques *via* specific binding to plaque-infiltrated macrophages. As shown in Figure 2, histology of the ^{99m}Tc-HFn-positive plaque region from the excised aorta showed intense macrophage infiltration (Mac-3 staining) and a strong correlation between ^{99m}Tc-HFn uptake and the extent of macrophage infiltration within plaques (***$P < 0.001$, $r^2 = 0.83$; Figure 2a). Immunofluorescent staining of the ^{99m}Tc-HFn-positive plaque region demonstrated colocalization of HFn staining with macrophages (Mac-3 staining; Figure 2b), indicating that HFn specifically binds to macrophages within plaques. We further isolated the plaque-infiltrated CD11b$^+$F4/80$^+$ macrophage cells and characterized their binding specificity with HFn (Figure 2c). The binding of HFn to plaque macrophages was saturable and could be inhibited by adding an excess of unlabeled HFn (Figure 2d, left), confirming the binding specificity of HFn to plaque macrophages. The saturation binding curve and Scatchard analysis demonstrate that the K_d value for HFn is 54.2 nM and the total binding capacity B_{max} is 34.6×10^{-19} mol/cell (Figure 2d, right), indicating a high binding affinity and capacity of HFn for plaque-infiltrated macrophages. This is highly valuable because macrophage-rich inflammation is an obligatory component of active plaques and is particularly intense in the high-risk plaque.[28−30]

To further confirm the binding specificity of the ^{99m}Tc-HFn to macrophages *in vivo*, we injected fluorescein isothiocyanate (FITC)-labeled HFn (FITC-HFn) intravenously into Apoe$^{-/-}$ mice and characterized the plaque region from the excised aorta using fluorescent histology. As shown in Supplementary Figure S5, FITC-HFn signals (green) were colocalized to the Mac-3-positive macrophages (red, anti-Mac-3 staining) within plaques. This result further confirms that HFn nanocages accumulate in atherosclerotic plaques *via* specific binding to plaque-infiltrated macrophages.

Pharmacokinetics and biodistribution studies revealed a rapid blood clearance half-life ($t_{1/2\beta}$) of 2.32 min (Supplementary Figure S6) as well as high aorta-to-background ratios against vertebrae, heart, and muscle of 7.22, 3.54 and 9.75, respectively, at the imaging time point (Supplementary Table S1). This result proves that a clear vessel wall imaging can be obtained using ^{99m}Tc-HFn because of the low background uptake around the whole aorta from the aortic arch to the thoracic aorta and abdominal aorta.

Comparison of ^{99m}Tc-HFn and ^{18}F-FDG Imaging. ^{18}F-FDG PET has been used generally for noninvasive imaging of vascular inflammation. We next compared the *in vivo* performance of ^{99m}Tc-HFn with ^{18}F-FDG. We injected ^{18}F-FDG tracer intravenously into Apoe$^{-/-}$ mice ($n = 8$) and wild-type C57 mice ($n = 5$) and obtained PET images at 2 h postinjection (Supplementary Figure S7). ^{18}F-FDG accumulated in the organs with high metabolism or excretion, including the heart, brown adipose tissue, bladder, vertebrae, *etc*. In particular, ^{18}F-FDG uptake in the target adjacent vertebrae and myocardium was higher than the signals originated from aortic plaques in Apoe$^{-/-}$ mice, which makes the plaque uptake barely distinguishable from background signal. In contrast, intense focal ^{99m}Tc-HFn uptake was present at the site of aortic plaque with a clear neighboring background that demonstrates a discernible and quantifiable plaque uptake (Supplementary Figure S7a), as further confirmed by the biodistribution data (Supplementary Table S1). There is no quantitative analysis present for ^{18}F-FDG images because no discernible plaque uptake was observed in murine aorta (Supplementary Figure S7b), even from 16 consecutive tomographic images covering the entire murine aorta (Supplemental Figure 7c). Although ^{18}F-FDG imaging was hampered by the problem of high background signals, it remains an important measure of general vascular inflammation in the aorta and carotid arteries, providing complementary and distinct metabolic information to that of ^{99m}Tc-HFn uptake.

DOI: 10.1021/acsnano.8b04158
ACS Nano 2018, 12, 9300−9308

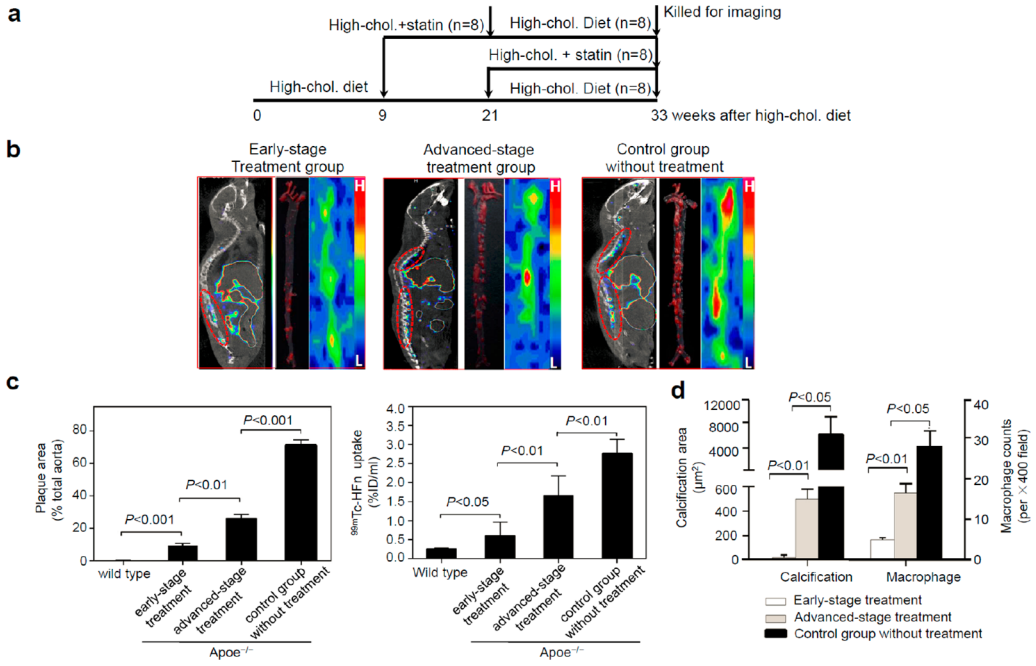

Figure 4. ^{99m}Tc-HFn uptake to monitor the dynamic changes of inflammation in mouse atherosclerotic plaques. (a) At 9 or 21 wk after a high-cholesterol diet, mice were randomized either to continue with the high-cholesterol diet or to consume the high-cholesterol diet admixed with an atorvastatin for 12 more weeks each. SPECT-CT imaging was performed at 33 wk in different treatment groups. (b) Representative images of *in vivo* ^{99m}Tc-HFn SPECT-CT imaging (left panels) in different treatment mice and the corresponding *ex vivo* planar imaging (right panels) and Oil Red O-stained aortas (middle panels) excised from mice after imaging with ^{99m}Tc-HFn. (c) Quantitative analysis of ^{99m}Tc-HFn uptake in aortas and plaque areas measured by Oil Red O staining of the aortas from different treatment groups. (d) Quantitative analysis of infiltrated macrophages (the number of Mac-3 positive cells per 10 high-power fields (×400) in plaques) and active calcification (positive area of von Kossa staining) within plaques of different treatment groups. **P* < 0.05 for control *versus* advanced-stage treatment group; ***P* < 0.01 for early stage treatment *versus* advanced-stage treatment group (*n* = 6 per group; 3 sections per aortic plaque region; unpaired Student's *t* test).

Combining of ^{99m}Tc-HFn and ^{18}F-NaF Imaging. Active calcification is another major characteristic of vulnerable atherosclerotic plaques, which is strongly associated with vascular inflammation, and they both largely drive atherosclerotic plaque progression and rupture. A comprehensive understanding and characterization of inflammatory infiltration and active calcification of atherosclerotic plaques offer complementary information for identifying plaque vulnerability. Many studies have recently shown the feasibility of ^{18}F-NaF to detect active calcification.[31−33] We therefore investigated whether ^{99m}Tc-HFn could be combined with ^{18}F-NaF to monitor inflammatory infiltration together with active calcification during the progression of atherosclerosis. We imaged plaque calcification activity in the aortas excised from atherosclerotic and control mice 2 h postintravenous administration of ^{18}F-NaF. As shown in Supplementary Figure S8, no significant ^{18}F-NaF uptake was detected in whole aortas from atherosclerotic mice at 12 wk after initiation of the atherogenic diet along with high ^{99m}Tc-HFn uptake. This demonstrates that inflammatory infiltration within plaques occurred earlier than calcification, indicating that ^{99m}Tc-HFn is a better targeted radiotracer than ^{18}F-NaF for identifying early active atherosclerosis. In later stages of the disease, both intense ^{99m}Tc-HFn and ^{18}F-NaF activities were observed at the sites of atherosclerotic lesions (Figure 1c, Supplementary Figure S8a), indicating both severe inflammatory infiltration and calcification deposition occurred within the plaques. ^{99m}Tc-HFn is therefore more favorable for monitoring the initiation of active ongoing plaques than ^{18}F-NaF, and the combined ^{99m}Tc-HFn and ^{18}F-NaF can monitor the inflammatory infiltration together with active calcification in latter stages of the disease.

In the following histological validation, we further identified no active calcification by von Kossa staining at the 12 wk time point section, while exhibiting obvious macrophage staining in the corresponding serial sections (Figure 3, top). With disease progression and severity, advanced plaques at 20 and 33 wk represent both prominent calcification activity and increased macrophage burden (Figure 3, middle and bottom). Therefore, ^{99m}Tc-HFn and ^{18}F-NaF can complement each other for atherosclerosis characterization by imaging plaque inflammation and active calcification, respectively, throughout the whole progression of atherosclerosis.

Monitoring of Anti-inflammatory Treatment with ^{99m}Tc-HFn in Atherosclerosis. In current clinical settings, patients with plaques are usually treated with statin anti-inflammatory therapy for prevention and treatment of coronary and carotid artery diseases. Therefore, quantitative monitoring of the anti-inflammatory treatment by using noninvasive imaging helps guide the current treatment strategies and assist in the development of novel treatment drugs.

We assessed the statin therapeutic effects on early and advanced stage atherosclerosis (9 and 21 wk after an atherogenic diet) in Apoe$^{-/-}$ mice by subjecting each of them to a 12 wk treatment (Figure 4a). ^{99m}Tc-HFn uptake was used to monitor the dynamic changes of inflammation in atherosclerotic plaques during plaque progression and anti-inflammatory treatment. Early stage treatment significantly

DOI: 10.1021/acsnano.8b04158
ACS Nano 2018, 12, 9300−9308

prevented the progression of atherosclerosis as compared with the control group without statin treatment, while less significant effects were observed in the advanced-stage treatment group (Figure 4b,c). Histology identified that the macrophage burden and calcification activity were also prevented more effectively by statin therapy in early atherosclerosis than advanced stage treatment (Figure 4d). Thus, early initiation of statin treatment is crucial to plaque formation prevention, since inflammation occurs in early stages of atherosclerosis. Furthermore, this indicates that ^{99m}Tc-HFn uptake can provide a useful approach to assess antiatherosclerotic therapy.

DISCUSSION

Natural human ferritin and its binding receptor, TfR1, are known to accumulate greatly in the infiltrated macrophages within atherosclerotic plaques and are significantly associated with increased risk of plaque rupture.[22] We identified that the bioengineered H-ferritin bound to the plaque-infiltrated macrophages with high specific binding affinity (K_d = 54.2 nM) and capacity (B_{max} = 34.6 × 10^{-19} mol/cell). By utilizing the intrinsic macrophage-binding property, we demonstrated that ^{99m}Tc-HFn can identify vulnerable plaques and early active ongoing plaques in living mice *via* combined SPECT and CT. Intensive focal ^{99m}Tc-HFn uptake was observed in the atherosclerotic plaques, which is associated with high-risk histological features of active calcification, macrophage infiltration, positive remodeling, and necrosis; these observations were made in the early active plaques with prominent macrophage infiltration as well. Furthermore, the dynamic changes of inflammation in plaques during anti-inflammation treatment was quantitatively monitored by ^{99m}Tc-HFn uptake. ^{99m}Tc-HFn therefore holds a major promise for identifying high-risk atheroma and potentially assessing anti-atherosclerotic therapy.

^{99m}Tc-HFn SPECT represents an advance for prevention and treatment of atherosclerosis and may have a medical impact for the following reasons: (1) Identification of vulnerable plaques: The current diagnostic strategies still cannot identify high-risk vulnerable plaques before they rupture and subsequent clinical symptoms appear. Therefore, patients get treatment after atherosclerotic plaque rupture initiates myocardial and cerebral infarctions, which remains the leading cause of death worldwide. ^{99m}Tc-HFn can identify and accurately localize vulnerable atherosclerotic plaques in living mice by specifically binding to plaque-infiltrated macrophages, which thus represents a potential clinical advance for prevention and treatment of coronary and carotid artery diseases. (2) Evaluation of statin prescribing: In current clinical settings, patients with plaques are usually treated with statin anti-inflammatory therapy for prevention and treatment of coronary and carotid artery diseases. Therefore, quantitative monitoring of the anti-inflammatory treatment by using noninvasive imaging would guide the current treatment strategies and assist the development of novel treatment drugs. ^{99m}Tc-HFn imaging enables quantitative monitoring of the dynamic changes of inflammation during plaque progression *in vivo* as well as assessing anti-inflammation therapy, and thus has a potential medical impact on the treatment of atherosclerosis.

Although there are several types of nanomaterials, such as iron oxide and gold NPs coated with dextran or high-density lipoprotein, that have been reported for imaging macrophages in atherosclerosis,[34−36] the bioengineered HFn nanocages described herein present the following points of advantages over existing nanoprobes: (1) Specificity: Most macrophage-specific NPs rely on their natural endocytoses, which are predominantly internalized by circulating monocytes and tissue macrophages in lymph nodes, liver, spleen, and bone marrow.[34] On the other hand, HFn nanocages bind to plaque macrophages through TfR1-mediated specific targeting, showing clear vessel wall imaging with little background uptake including the target adjacent bone marrow (Figure 1a and Table S1). (2) Biodegradability: Most macrophage-specific NPs are relatively large, 10−300 nm in diameter, and typically nonbiodegradable.[35,36] Therefore, these NPs accumulate nonspecifically in the reticuloendothelial system, including the spleen and liver, and are potentially toxic to the immune system. HFn nanocages exist naturally in humans and are composed of nontoxic globular proteins (8−12 nm); therefore, they would not activate inflammatory or immunological responses.[25−27] (3) Simplicity: HFn nanocages are produced from *Escherichia coli* at a high yield (>100 mg/L from the bacterial lysate) and can be used for further modification with radiolabeling or fluorescence labeling.[25,26]

CONCLUSIONS

There is an unmet clinical need to develop radiotracers that can identify vulnerable and early active atherosclerotic plaques to prevent and treat myocardial infarction and ischemic stroke. In this study, we demonstrated the specific uptake of iron-storage nanocage HFn to the infiltrated macrophages within the high-risk plaques as well as in early active ongoing atherosclerotic plaques. The high target specificity, low myocardial and background activities, and high sensitivity for vulnerable and early active plaques give advantages to ^{99m}Tc-HFn over the use of ^{18}F-FDG for atherosclerosis imaging. The ability to monitor plaque progression and treat it with anti-inflammatory interventions supports the vascular ^{99m}Tc-HFn uptake as a potential noninvasive imaging radiotracer to identify high-risk atheroma and potentially assess anti-atherosclerotic therapy.

MATERIALS AND METHODS

Preparation and Characterization of ^{99m}Tc-HFn. Human HFn was produced in *E. coli* and purified as previously described.[25,26] *N*-Hydroxysuccinimidyl *S*-acetylmercaptoacetyltriglycinate (NHS-MAG_3) was synthesized in-house and conjugated to HFn *via* the derivatized amine as previously described.[37] MAG_3-conjugated HFn (MAG_3-HFn) was radiolabeled with ^{99m}Tc-pertechnetate ($^{99m}TcO_4^-$) (Shanghai GMS Pharmaceutical Co., Ltd.) by the following procedure. Briefly, a solution of 100 μg of MAG_3-HFn conjugates in 45 μL of ammonium acetate (0.25 M) was added to 15 μL of tartrate buffer with 37 MBq of $^{99m}TcO^{4-}$. After vortexing, 4 μL of freshly prepared 1 mg/mL $SnCl_2{\cdot}2H_2O$ solution was added. The mixture was incubated for 1 h at room temperature under vortexing. The final radiochemical yield of ^{99m}Tc-HFn was >98%. The labeling yield and radiochemical purity of the products were measured by instant thin-layer chromatography (ITLC) on a radio thin-layer scanner (Bioscan).

Animals. We used atherosclerotic apolipoprotein E knockout ($ApoE^{-/-}$) mice (C57BL/6J background) for plaque imaging and therapeutic studies. Mice were fed with an atherogenic diet (containing 21% fat and 0.15% cholesterol by weight) starting at 9 wk of age. After consuming the atherogenic diet for 12, 20, or 33 wk, mice were used for imaging experiments. Therapeutic groups were given 12 wk of atorvastatin therapy with 10 mg/kg/d at 9 or 21 wk after beginning the atherogenic diet. Age-matched wild-type C57BL/

DOI: 10.1021/acsnano.8b04158
ACS Nano 2018, 12, 9300−9308

6J mice on normal chow were used as disease controls. All animals were fasted overnight before use for imaging experiments. Protocols were performed with the approval of the Ethical Committee of Zhongshan Hospital, Fudan University.

^{99m}Tc-HFn SPECT-CT Imaging. Atherosclerotic and control mice were intravenously administrated ^{99m}Tc-HFn with a dose of 500 μCi (^{99m}Tc) and 100 μg (HFn) per mouse in 100 μL of saline. Two hours after injection, anesthetized mice were imaged on a small-animal nano-SPECT/CT system (Bioscan). SPECT and CT acquisitions were reconstructed, fused, and quantified using dedicated software, InVivoScope (version 1.43, Bioscan). Spatial resolution was 1 mm/pixel for SPECT imaging. Regions of interest (ROIs) were manually drawn in the aorta where obvious radioactivity was present. SPECT scale was normalized to %ID/mL to allow direct visual comparison between animals. The high background uptake of liver and bladder were automatically removed from the images by the postprocessing software (InVivoScope; Invicro, Boston, MA, USA).

After *in vivo* imaging, the mice were sacrificed and aortas were immediately excised for *ex vivo* planar imaging using a gamma camera (Dilon 6800, Dilon Technologies) with the following parameters: collimator, low-energy general-purpose; peak energy, 140 keV; window width, ±10%; matrix, 80 × 80; resolution, 0.32 mm/pixel. The collection time was 30 min with total counts of 80 000−100 000.

^{18}F-FDG and ^{18}F-NaF PET Imaging. Atherosclerotic and control mice were intravenously injected with 200 μCi of ^{18}F-FDG or ^{18}F-NaF per mouse in 100 μL of saline. Mice were anesthetized with 2% isoflurane inhalation 2 h postinjection and imaged on a Nano PET scanner (Shandong Madic Technology, China). Depending on the count rate, PET images were acquired for 20 min and then reconstructed using a two-dimensional ordered-subset expectation maximum (2D OSEM) algorithm. Spatial resolution was 2 mm/pixel for PET imaging. After *in vivo* imaging, the mice were sacrificed and aortas were excised and imaged on a PET scanner using the following parameters: transaxial FOV in 80 mm, axial FOV in 59 mm, spatial resolution less than 1.3 mm, scatter fraction 6.3%. ROI was drawn in the aorta, and the mean of standard uptake values was automatically generated by the software for each ROI.

Oil Red O Staining of Aorta. Lipid deposition within the aortas (fixed with 10% formalin) was determined by Oil Red O staining. Briefly, the dissected aorta was opened longitudinally and fixed in 10% formalin for 5−10 min. The fixed aortas were rinsed with 60% propylene glycol for 10 min and then stained with 0.5% Oil Red O solution (in propylene glycol) for 30 min at 37 °C. Finally, the aortas were differentiated with 60% propylene glycol solution for 5 min. Lipids were stained in red. The stained aortas were spread on a black charpie for photographing using a digital camera under identical light conditions with the same photographing parameters. Pictures were analyzed with Image Pro Plus (version 6.0, Media Cybernetics). The quantified results were expressed as the ratio of percentages of the lipid-accumulating lesion area to the total aortic area.

Histopathological Analysis. After imaging and radioactivity counting, aortas were fixed in formalin, dehydrated, embedded in paraffin, and sliced in the region of the aortic arch, thoracic aorta, and abdominal aorta that presented obvious plaques. Tissue samples were cut into serial sections 5 μm thick and stained with hematoxylin and eosin for general morphology. For immunohistochemistry analysis, corresponding neighboring sections were stained overnight at 4 °C using primary anti-Mac3 antibody (BD Biosciences) for macrophage detection. Then the primary antibody was detected by incubating the sections with a biotinylated secondary antibody (Santa Cruz Biotech) and with an avidin−biotinylated horseradish peroxidase complex solution according to the manufacturer's directions. Finally, peroxidase activity was revealed by immersion in diaminobenzidine. Digital images of the stained sections were obtained with a scanning light microscope (Leica Microsystems). For von Kossa staining, sections were stained in 1% silver nitrate solution under ultraviolet light for 20 min, then incubated in 5% sodium thiosulfate, and counterstained with Eosin Y. For immunofluorescence staining, serial sections were incubated overnight with FITC-conjugated HFn or a Cy5.5-conjugated anti-Mac3 antibody (BD Biosciences). The nuclei were counterstained with 4′,6-diamidino-2-phenylindole. The stained tissues were examined under a confocal laser scanning microscope (Olympus).

Macrophage Binding Studies. We isolated F4/80+ CD11b+ macrophages from atherosclerotic plaques from ApoE$^{-/-}$ mice that consumed the atherogenic diet for 33 wk. The macrophage binding affinity of ^{99m}Tc-HFn was determined by saturation binding experiments using previously described methods with some modifications.[24] The freshly isolated macrophages were seeded in a Millipore 96-well filter plate (10^5 per well), then incubated with increasing concentrations of ^{99m}Tc-HFn (4, 8, 12, 24, 32, 96, and 192 nM) at 37 °C for 2 h. The total volume of each well was adjusted to 200 μL of 1% bovine serum albumin in phosphate-buffered saline (PBS). After incubation, the cells were filtered, washed three times with PBS, and collected, and the radioactivity was determined using a gamma counter (CRC-15 R, Capintec Inc., Ramsey, NJ, USA). Nonspecific binding was determined in the presence of an excess of cold HFn (>100-fold). A saturation binding curve and Scatchard transformation were obtained by nonlinear regression analysis, and the K_d and B_{max} (maximum number of binding sites) values of ^{99m}Tc-HFn were calculated using GraphPad Prism 6.0 software. All experimental conditions were triplicate.

Statistical Analyses. All statistical analyses were performed with SPSS19.0 (IBM, Chicago, IL, USA) and GraphPad Prism 5.01 (GraphPad Software Inc.) software. Results were expressed as mean ± SD. Unpaired Student's *t* tests were performed to evaluate the significance of differences between groups. We considered a *P* value of <0.05 as statistically significant. Correlations between ^{99m}Tc-HFn uptake and plaque areas were determined using the Pearson coefficient (*r*) and *P* value.

ASSOCIATED CONTENT

Supporting Information

The Supporting Information is available free of charge on the ACS Publications website at DOI: 10.1021/acsnano.8b04158.

Detailed descriptions for the characterization of ^{99m}Tc-HFn, stability experiment, tissue staining, *in vivo* imaging, blood clearance, and biodistribution studies (PDF)

AUTHOR INFORMATION

Corresponding Authors

*D. Cheng, E-mail: cheng.dengfeng@zs-hospital.sh.cn. Tel: +86 21 6404-1990.

*H. Shi, E-mail: shi.hongcheng@zs-hospital.sh.cn. Tel: +86 21 6404-1990.

*H. S. Choi, E-mail: hchoi12@mgh.harvard.edu. Tel: +1 617-726-5784.

*X. Yan, E-mail: yanxy@ibp.ac.cn. Tel: +86 10-6488-8583. Fax: +86 10-6488-8584.

ORCID

Minmin Liang: 0000-0002-5152-5240

Kelong Fan: 0000-0001-6285-1933

Hak Soo Choi: 0000-0002-7982-6483

Xiyun Yan: 0000-0002-7290-352X

Author Contributions

#M. Liang and H. Tan contributed equally to this work.

Author Contributions

M.L. and D.C.conceived and designed the experiments. D.C. H.T., and M.L. performed the experiments. M.L, D.C., H.S.C., and X.Y. reviewed, analyzed, and interpreted the data. M.L., D.C., and H.S.C. wrote the paper. All authors discussed the results and commented on the manuscript.

DOI: 10.1021/acsnano.8b04158
ACS Nano 2018, 12, 9300−9308

Notes

The authors declare no competing financial interest.

ACKNOWLEDGMENTS

We thank Ivey Choi for manuscript editing. This work was supported by the following grants: National Key R&D Program of China (2017YFA0205501), National Natural Science Foundation of China (81722024, 81571728, 81471706, 81671735, 81571728), Key Research of Frontier Sciences (QYZDY-SSW-SMC013), Strategic Priority Research Program of Chinese Academy of Sciences (XDA09030306, XDPB0304), Shanghai Science and Technology Committee International Collaboration Project (16410722700), and Youth Innovation Promotion Association of Chinese Academy of Sciences (2014078).

REFERENCES

(1) Lozano, R.; Naghavi, M.; Foreman, K.; Lim, S.; Shibuya, K.; Aboyans, V.; Abraham, J.; Adair, T.; Aggarwal, R.; Ahn, S. Y. Global and Regional Mortality from 235 causes of Death for 20 Age Groups in 1990 and 2010: A Systematic Analysis for the Global Burden of Disease Study 2010. *Lancet* **2012**, *380*, 2095−2128.

(2) Naghavi, M.; Libby, P.; Falk, E.; Casscells, S. W.; Litovsky, S.; Rumberger, J.; Badimon, J. J.; Stefanadis, C.; Moreno, P.; Pasterkamp, G. From Vulnerable Plaque to Vulnerable Patient: A Call for New Definitions and Risk Assessment Strategies: Part I. *Circulation* **2003**, *108*, 1664−1672.

(3) Virmani, R.; Kolodgie, F. D.; Burke, A. P.; Farb, A.; Schwartz, S. M. Lessons from Sudden Coronary Death: A Comprehensive Morphological Classification Scheme for Atherosclerotic Lesions. *Arterioscler., Thromb., Vasc. Biol.* **2000**, *20*, 1262−1275.

(4) Virmani, R.; Burke, A. P.; Farb, A.; Kolodgie, F. D. Pathology of the Vulnerable Plaque. *J. Am. Coll. Cardiol.* **2006**, *47* (suppl), C13−18.

(5) Rogers, I. S.; Tawako, A. Imaging of Coronary Inflammation with FDG-PET: Feasibility and Clinical Hurdles. *Curr. Cardiol. Rep.* **2011**, *13*, 138−144.

(6) Libby, P.; DiCarli, M.; Weissleder, R. The Vascular Biology of Atherosclerosis and Imaging Targets. *J. Nucl. Med.* **2010**, *51*, 33S−37S.

(7) Rogers, I. S.; Nasir, K.; Figueroa, A. L.; Cury, R. C.; Hoffmann, U.; Vermylen, D. A.; Brady, T. J.; Tawakol, A. Feasibility of FDG Imaging of the Coronary Arteries: Comparison between Acute Coronary Syndrome and Stable Angina. *JACC Cardiovasc. Imag.* **2010**, *3*, 388−397.

(8) Dweck, M. R.; Chow, M. W.; Joshi, N. V.; Williams, M. C.; Jones, C.; Fletcher, A. M.; Richardson, H.; White, A.; McKillop, G.; van Beek, E. J. Coronary Arterial ^{18}F-Sodium Fluoride Uptake: A Novel Marker of Plaque Biology. *J. Am. Coll. Cardiol.* **2012**, *59*, 1539−1548.

(9) Libby, P. Inflammation in Atherosclerosis. *Nature* **2002**, *420*, 868−874.

(10) Aikawa, E.; Nahrendorf, M.; Figueiredo, J. L.; Swirski, F. K.; Shtatland, T.; Kohler, R. H.; Jaffer, F. A.; Aikawa, M.; Weissleder, R. Osteogenesis Associates with Inflammation in Early-Stage Atherosclerosis Evaluated by Molecular Imaging In Vivo. *Circulation* **2007**, *116*, 2841−2850.

(11) Hutcheson, J. D.; Goettsch, C.; Bertazzo, S.; Maldonado, N.; Ruiz, J. L.; Goh, W.; Yabusaki, K.; aits, T.; Bouten, C.; Franck, G. Genesis and Growth of Extracellular-Vesicle-Derived Microcalcification in Atherosclerotic Plaques. *Nat. Mater.* **2016**, *15*, 335−343.

(12) Dweck, M. R.; Jones, C.; Joshi, N. V.; Fletcher, A. M.; Richardson, H.; White, A.; Marsden, M.; Pessotto, R.; Clark, J. C.; Wallace, W. A. Assessment of Valvular Calcification and Inflammation by Positron Emission Tomography in Patients with Aortic Stenosis. *Circulation* **2012**, *125*, 76−86.

(13) Joshi, N. V.; Vesey, A. T.; Williams, M. C.; Shah, A. S.; Calvert, P. A.; Craighead, F. H.; Yeoh, S. E.; Wallace, W.; Salter, D.; Fletcher, A. M. ^{18}F-Fluoride Positron Emission Tomography for Identification of Ruptured and High-Risk Coronary Atherosclerotic Plaques: A Prospective Clinical Trial. *Lancet* **2014**, *383*, 705−713.

(14) Irkle, A.; Vesey, A. T.; Lewis, D. Y.; Skepper, J. N.; Bird, J. L.; Dweck, M. R.; Joshi, F. R.; Gallagher, F. A.; Warburton, E. A.; Bennett, M. R. Identifying Active Vascular Microcalcification by ^{18}F-Sodium Fluoride Positron Emission Tomography. *Nat. Commun.* **2015**, *6*, 7495.

(15) Rudd, J. H.; Warburton, E. A.; Fryer, T. D.; Jones, H. A.; Clark, J. C.; Antoun, N.; Johnström, P.; Davenport, A. P.; Kirkpatrick, P. J.; Arch, B. N. Imaging Atherosclerotic Plaque Inflammation with [^{18}F]-Fluorodeoxyglucose Positron Emission Tomography. *Circulation* **2002**, *105*, 2708−2711.

(16) Tarkin, J. M.; Joshi, F. R.; Rudd, J. H. PET Imaging of Inflammation in Atherosclerosis. *Nat. Rev. Cardiol.* **2014**, *11*, 443−457.

(17) Joshi, N. V.; Vesey, A.; Newby, D. E.; Dweck, M. R. Will ^{18}F-sodium Fluoride PET-CT Imaging be the Magic Bullet for Identifying Vulnerable Coronary Atherosclerotic Plaques? *Curr. Cardiol. Rep.* **2014**, *16*, 521.

(18) Chen, W.; Dilsizian, V. Targeted PET/CT Imaging of Vulnerable Atherosclerotic Plaques: Microcalcification with Sodium Fluoride and Inflammation with Fluorodeoxyglucose. *Curr. Cardiol. Rep.* **2013**, *15*, 364.

(19) Theil, E. C. Ferritin: Structure, Gene Regulation, and Cellular Function in Animals, Plants, and Microorganisms. *Annu. Rev. Biochem.* **1987**, *56*, 289−315.

(20) Arosio, P.; Ingrassia, R.; Cavadini, P. Ferritins: A family of Molecules for Iron Storage, Antioxidation and More. *Biochim. Biophys. Acta, Gen. Subj.* **2009**, *1790*, 589−599.

(21) Lawson, D. M.; Artymiuk, P. J.; Yewdall, S. J.; Smith, J. M.; Livingstone, J. C.; Treffry, A.; Luzzago, A.; Levi, S.; Arosio, P.; Cesareni, G. Solving the Structure of Human H Ferritin by Genetically Engineering Intermolecular Crystal Contacts. *Nature* **1991**, *349*, 541.

(22) Li, W.; Xu, L. H.; Forssell, C.; Sullivan, J. L.; Yuan, X. M. Overexpression of Transferrin Receptor and Ferritin Related to Clinical Symptoms and Destabilization of Human Carotid Plaques. *Exp. Biol. Med.* **2008**, *233*, 818−826.

(23) Kraml, P.; Potocková, J.; Koprivová, H.; Stípek, S.; Crkovská, J.; Zima, T.; Anděl, M. Ferritin, Oxidative Stress and Coronary Atherosclerosis. *Vnitr. Lek.* **2004**, *50*, 197−202.

(24) Terashima, M.; Uchida, M.; Kosuge, H.; Tsao, P. S.; Young, M. J.; Conolly, S. M.; Douglas, T.; McConnell, M. V. Human Ferritin Cages for Imaging Vascular Macrophages. *Biomaterials* **2011**, *32*, 1430−1437.

(25) Fan, K.; Cao, C.; Pan, Y.; Lu, D.; Yang, D.; Feng, J.; Song, L.; Liang, M.; Yan, X. Magnetoferritin Nanoparticles for Targeting and Visualizing Tumour Tissues. *Nat. Nanotechnol.* **2012**, *7*, 459−464.

(26) Liang, M.; Fan, K.; Zhou, M.; Duan, D.; Zheng, J.; Yang, D.; Feng, J.; Yan, X. H-Ferritin-Nanocaged Doxorubicin Nanoparticles Specifically Target and Kill Tumors with a Single-Dose Injection. *Proc. Natl. Acad. Sci. U. S. A.* **2014**, *111*, 14900−14905.

(27) Zhao, Y.; Liang, M.; Li, X.; Fan, K.; Xiao, J.; Li, Y.; Shi, H.; Wang, F.; Choi, H. S.; Cheng, D. Bioengineered Magnetoferritin Nanoprobes for Single-Dose Nuclear-Magnetic Resonance Tumor Imaging. *ACS Nano* **2016**, *10*, 4184−4191.

(28) Libby, P.; Ridker, P. M.; Maseri, A. Inflammation and Atherosclerosis. *Circulation* **2002**, *105*, 1135−1143.

(29) Tabas, I.; Glass, C. K. Anti-inflammatory Therapy in Chronic Disease: Challenges and Opportunities. *Science* **2013**, *339*, 166−172.

(30) Moore, K. J.; Sheedy, F. J.; Fisher, E. A. Macrophages in Atherosclerosis: A Dynamic Balance. *Nat. Rev. Immunol.* **2013**, *13*, 709−721.

(31) Dweck, M. R.; Khaw, H. J.; Sng, G. K.; Luo, E. L.; Baird, A.; Williams, M. C.; Makiello, P.; Mirsadraee, S.; Joshi, N. V.; van Beek, E. J. Aortic Stenosis, Atherosclerosis, and Skeletal Bone: Is There a

DOI: 10.1021/acsnano.8b04158
ACS Nano 2018, 12, 9300−9308

Common Link with Calcification and Inflammation? *Eur. Heart J.* **2013**, *34*, 1567−1574.
(32) New, S. E.; Aikawa, E. Cardiovascular Calcification. *Circ. J.* **2011**, *75*, 1305−1313.
(33) Nakahara, T.; Narula, J.; Strauss, H. W. Calcification and Inflammation in Atherosclerosis. *J. Am. Coll. Cardiol.* **2016**, *67*, 79−80.
(34) Lobatto, M. E.; Calcagno, C.; Millon, A.; Senders, M. L.; Fay, F.; Robson, P. M.; Ramachandran, S.; Binderup, T.; Paridaans, M. P.; Sensarn, M. S.; Rogalla, S.; Gordon, R. E.; Cardoso, L.; Storm, G.; Metselaar, J. M.; Contag, C. H.; Stroes, E. S. G.; Fayad, Z. A.; Mulder, W. J. M. Atherosclerotic Plaque Targeting Mechanism of Long-Circulating Nanoparticles Established by Multimodal Imaging. *ACS Nano* **2015**, *9*, 1837−1847.
(35) Lobatto, M. E.; Fuster, V.; Fayad, Z. A.; Mulder, W. J. M. Perspectives and Opportunities for Nanomedicine in the Management of Atherosclerosis. *Nat. Rev. Drug Discovery* **2011**, *10*, 835−852.
(36) Cormode, D. P.; Roessl, E.; Thran, A.; Skajaa, T.; Gordon, R. E.; Schlomka, J. P.; Fuster, V.; Fisher, E. A.; Mulder, W. J. M.; Proksa, R.; Fayad, Z. A. Atherosclerotic Plaque Composition: Analysis with Multicolor CT and Targeted Gold Nanoparticles. *Radiology* **2010**, *256*, 774−782.
(37) Wang, Y.; Liu, G.; Hnatowich, D. J. Methods for MAG_3 Conjugation and ^{99m}Tc Radiolabeling of Biomolecules. *Nat. Protoc.* **2006**, *1*, 1477−1480.

DOI: 10.1021/acsnano.8b04158
ACS Nano 2018, 12, 9300−9308